Advances in Water Resources 202 (2025) 104998

Contents lists available at ScienceDirect

Advances in Water Resources

journal homepage: www.elsevier.com/locate/advwatres

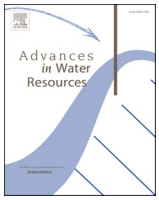

Pore-scale investigations of particle migration by fluid–particle interactions in immiscible two-phase flow systems: A three-dimensional X-ray microtomography study

Sotheavuth Sin [a,*], Muhammad Nasir [a], Kailin Wang [a], Aninditya Patmonoaji [b], Wilson Susanto [a], Bowen Wang [a], Shintaro Matsushita [a], Tetsuya Suekane [a]

[a] Department of Mechanical Engineering, Institute of Science Tokyo, 2-12-1 Ookayama, Meguro-ku, Tokyo, 152-8550, Japan
[b] Department of Earth Science and Engineering, Imperial College London, United Kingdom

ARTICLE INFO

Keywords:
Particle migration
Interface behavior
Wettability
Immiscible two-phase flow
X-ray computed tomography (CT)

ABSTRACT

Understanding of particle migration by fluid–particle interactions in immiscible two-phase flow systems in porous media is crucial for subsurface applications. However, pore-scale investigations of particle migration in immiscible two-phase flow systems remain limited for three-dimensional (3D) porous media because of the complexities of fluid flow in such media. Here, we employed microfocus X-ray computed tomography (CT) to investigate the effects of interfacial tension and viscous force on particle migration during fluid–particle interactions in strong drainage and imbibition for the pore-scale process. A mixture of two differently sized particles was used as a 3D heterogeneous porous medium. The experimental conditions cover the logarithmic values of the capillary number (Log*Ca*) range between −7.476 and −4.777 and of a fixed viscosity ratio (Log*M*) of −0.867, which are used to simulate the carbon dioxide (CO_2) sequestration. The results show that particle migration significantly proceeded throughout the medium for strong drainage compared to strong imbibition. At a low injection flow rate or Log*Ca*, interfacial tension strongly influenced particle accumulation, altering pore networks. The combined effects of interfacial tension and viscous force enhanced particle migration with an increase in Log*Ca*. In strong drainage, the particles migrated with the interface expansion between the two phases. However, in strong imbibition, they were displaced along with the fluid flow because of the presence of film formations. The findings of this study improve the understanding of particle migration by fluid–particle interactions under different injection flow rates and wettability conditions in 3D heterogeneous porous media.

1. Introduction

Particle or fines migration has been extensively investigated in single- and two-phase flows over the past decades because of its diverse subsurface applications, such as hydrology (Russell et al., 2018; Wang et al., 2022a), carbon capture and storage (CCS) (Chen et al., 2023; Ge et al., 2022; Wang et al., 2022b; Xie et al., 2017), oil and gas production (Alhammadi et al., 2020; Almutairi et al., 2023; Han et al., 2020, 2018; Tang and Morrow, 1999; Xie et al., 2023; Zhu et al., 2017), hydraulic fracturing (Boronin and Osiptsov, 2014; Derbyshev et al., 2024), and suffusion in gap-graded soils (Ke and Takahashi, 2014; Nguyen et al., 2019; Xu et al., 2024). For CCS processes, a large amount of CO_2 emissions from the industry sector is injected into geological formations, such as depleted oil and gas reservoirs and deep saline aquifers. When CO_2 is injected into the negative buoyancy zone (NBZ) with a depth greater than 3.5 km (House et al., 2006; Qanbari et al., 2011; Schrag, 2007; Teng and Zhang, 2018), CO_2 will reside in its liquid phase at high pressure (35 MPa) and low temperature (3 °C) with a geothermal gradient of 0.03 K/m (Teng and Zhang, 2018). Under these typical conditions, the CO_2 density increased to 1027–1050 kg/m^3, and its viscosity is approximately 0.15 m Pas (Qanbari et al., 2011). The interfacial tension is about 30 mN/m (Shiga et al., 2023). The high-density CO_2 injection increased the interactions between the injected CO_2 and the formation of brine and rocks. One of the challenges for CO_2 injection in NBZ is the possibility of fractures or small-scale seismic events due to the changes of unconsolidated properties of the medium (e.g., porosity and permeability) and pore pressure during fines migration in the flow stream with high injection velocity (Zoback and

* Corresponding author.
E-mail address: sin.s.ab@m.titech.ac.jp (S. Sin).

https://doi.org/10.1016/j.advwatres.2025.104998
Received 28 November 2024; Received in revised form 2 April 2025; Accepted 22 April 2025
Available online 24 April 2025

Gorelick, 2012). Studies have revealed a decline in permeability caused by the migration and clogging of fine particles in narrow pore channels (Civan, 2010; Xie et al., 2017; Zeinijahromi et al., 2016). Therefore, it is important to understand the mechanisms of particle migration with the injected fluid under different reservoirs and injection conditions to optimize the CO_2 injection and storage efficiency and prevent possible risks such as formation damage or induced seismicity prior to CO_2 injection into NBZ.

In immiscible fluid–fluid displacement processes in porous media, i.e., drainage or imbibition, the two important dimensionless numbers that characterize fluid flow are the capillary number (Ca) and viscosity ratio (M) (Hu et al., 2020; Lenormand et al., 1988; Patmonoaji et al., 2020a). The Ca is the ratio of the viscous force to interfacial tension; $Ca = v_{IP}\mu_{IP}/\gamma$, where v_{IP} and μ_{IP} are the characteristic velocity and viscosity of the invading phase (IP), while γ is the interfacial tension. Here, the characteristic velocity $v_{IP} = Q/\phi A$ depends on the flow rate (Q), the porosity (ϕ) and the cross-sectional area of the packed bed (A). The M is the ratio of μ_{IP} to the viscosity of the defending phase (DP) (μ_{DP}); $M = \mu_{IP}/\mu_{DP}$. A two-phase flow displacement diagram was developed using the relations of Log$M$-LogCa, showing the displacement regimes among the viscous fingering (VF) or unfavorable displacement (Log$M$ < 0), capillary fingering (CF), and stable or favorable displacement (Log$M$ > 0) (Hu et al., 2020; Lenormand et al., 1988; Zhang et al., 2011) (Fig. 1S). The fluid–fluid displacement for each regime influences particle migration differently, as the displacement relies on the competition between the forces. For example, the transition of CF and VF relies on the competition of viscous and capillary forces (Glass et al., 2003; Holtzman et al., 2012; Han et al., 2020; Patmonoaji et al., 2020a) and is influenced by the wetting conditions (Glass et al., 2003; Hu et al., 2017; Yang et al., 2019, 2016; Zhao et al., 2016). Holtzman et al. (2012) investigated capillary fracturing in granular media by injecting air into a thin bed of water-saturated glass beads. They observed that the difference in invasion morphology was related to the displacement of the beads in the cell, as the air–water interface in VF continuously grows, whereas it propagates intermittently in the CF. The invasion patterns of the combinations of the air–water system and granular suspensions in thin cells have been reported at varying injection rates and bead fractions (Chevalier et al., 2009; F.K. Eriksen et al., 2015; J.A. Eriksen et al., 2015). Meng et al. (2023) investigated the fluid-induced deformation and fracture of the water–oil system in cohesive granular media. They observed that the granular pack was dilated behind the water invasion front while it was compacted ahead of the water invasion front, indicating medium deformation due to particle or bead displacement. Most studies mainly discussed the evolution of invasion patterns between immiscible two-phase flow and fluid-particle interactions in two-dimensional (2D) homogeneous porous media by considering only two forces, i.e., capillary and viscous forces. However, it is expected that the invasion of injected fluid may exhibit different structures and fluid-particle interactions in 3D heterogeneous porous media because of the pore structure heterogeneity and the existence of additional forces (e.g., buoyancy force and gravity) in the system. 3D studies provide a more realistic representation of the flow and particle interactions for real porous media.

The translational motion of particles with injected fluid in immiscible two-phase flow systems is mainly characterized by various forces, such as (1) viscous or drag force by the friction at the fluid–particle interface, (2) interfacial tension force between the two phases, (3) pressure force by the fluid injection rate, (4) gravitational force, and (5) buoyancy force (Han et al., 2020; Shang et al., 2009; Sharma et al., 1992; Zeinijahromi et al., 2016). These forces influence the mechanisms of particle migration with injected fluid in 3D porous media. Viscous force and interfacial tension have a stronger impact on particle movement than other forces. The strength of the viscous and capillary forces relies on the flow rate conditions. At low flow rates, capillary force dominates due to interfacial tension, while at high flow rates, viscous force prevails in the system. Han et al. (2020) conducted one-dimensional porous channel experiments using sandy sediments with non-plastic silty fines to investigate the effects of fluid velocity and mixed fluid flows on pore clogging. They found that drag or viscous force significantly affected pore clogging in single-phase flow, while interfacial tension between gas and water promoted pore clogging in mixed two-phase flow. Jung et al. (2018) observed particle migration, bridging, and clogging behavior in a two-phase immiscible gas-water system through a microfluidic pore network using high-resolution microscopy. They found that fine particles aggregated near the two-phase interface, clogging pore throats and increasing particle concentrations within the pores. Once fine particles accumulated along the water-gas interface, additional mobile particles easily gathered around the existing ones. Huang et al. (2018) studied fines detachment mechanisms induced by single- and two-phase flow in fractured coal plugs, simulating coalbed methane reservoir porous media using scanning electron microscopy. They found that moving gas-water interfaces during early-stage two-phase flow significantly increased fines detachment compared to single-phase water flow. Fine particles detached and were released from the fracture surface as the gas-water interface advanced. However, when it receded, fines were released in the opposite direction.

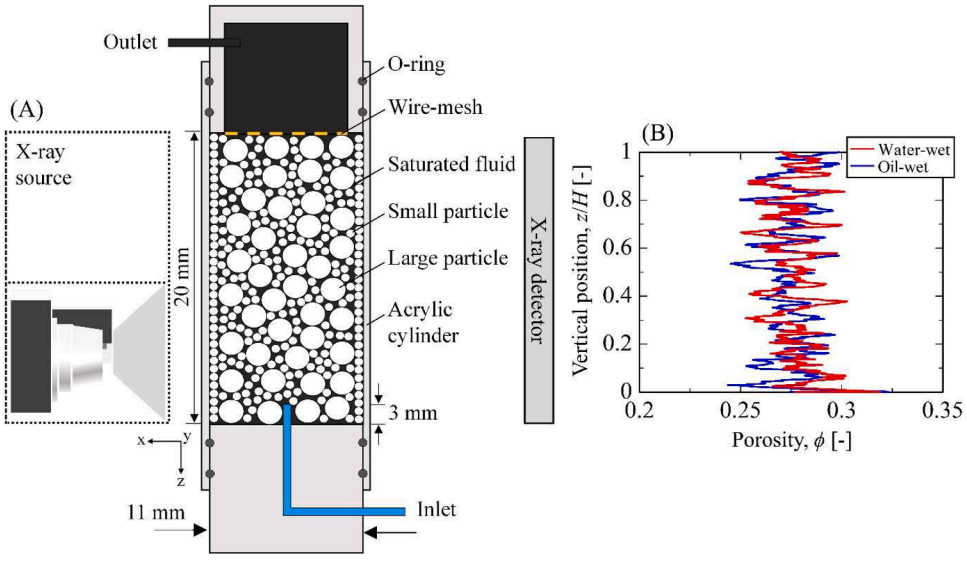

Fig. 1. (A) Schematic of the experimental setup and (B) porosity of water-wet and oil-wet porous media.

Conventional methods (e.g., bulk pressure and flow measurements) are inadequate for revealing key particle migration mechanisms, such as accumulation, clogging, interface behavior, and local porosity changes during pore-scale transport processes. The X-ray CT approach is well-suited for studying these mechanisms through direct visualizations (Iraji et al., 2024; Xu et al., 2024). To our knowledge, owing to their complexities, very few experimental studies have provided qualitative pore-scale visualizations of fluid-particle interactions to explain how particles migrate under varying injection flow rates and wettability conditions in 3D porous media.

By using an X-ray CT-based method, we investigated the effects of interfacial tension and viscous force on particle migration by fluid–particle interactions during the pore-scale transport process of strong drainage and imbibition in 3D heterogeneous porous media. The materials used in the experimental setup, procedures, and implemented image processing methods are described in the following section. Section 3 discusses the results of the study in two parts, namely "Drainage system" and "Imbibition system". Each system composes the results of the 3D structure of the invading fluid and its saturation profile at various injection flow rates, invasion front behavior of the invading fluid, effects of interfacial tension and viscous force on particle migration, changes in packing density in the medium, and evolution of injection pressure with the injected volume. Section 4 summarizes the conclusions of the study.

2. Material and methods

2.1. Porous media

A mixture of two differently sized glass beads (As-one Inc., Japan) was packed in an acrylic cylindrical tube with an inner diameter (d) of 11 mm and a height of 20 mm to represent a 3D heterogeneous porous medium for single- and two-phase flow experiments (Fig. 1(A)). Large and small glass beads represented coarse fraction grains and erodible fine particles within the voids of coarse grains. The average diameters of the large and small glass beads were $d_l = 1000$ μm (As one, BZ-1) and $d_s = 200$ μm (As one, BZ-02), respectively. The density of the glass beads was 2500 kg/m^3, and the shape of the beads was mainly round or spherical. The mixture of these particles contained 35% and 65% in mass of the small and large particles, respectively. The porous medium was internally unstable owing to internal erosion under continuous fluid flow when the particle mixture ratio exceeded 4 ($d_l/d_s > 4$) (Kezdi, 1979). Two porous media were created by altering their wettability, i.e., strong water-wet ($\theta \approx 19^\circ$) and strong oil-wet ($\theta \approx 141^\circ$). The detailed wettability alteration was given in the supplementary material. The porosities of both porous media were identical and estimated to be approximately 0.278 ± 0.012 (Fig. 1(B)), which is the average value over all samples, with variations from 0.268 to 0.312 (Table 1S). Porosity variations of 10–20% between single- and two-phase flow experiments significantly affect permeability of the medium, influencing viscous forces on particle migration. These variations also affect fluid distribution and pressure gradients during flow. Thus, considering vertical variations is crucial for minimizing inconsistencies and ensuring accurate experimental results. The porosity of the porous medium (ϕ) was estimated as the ratio of the void fraction to the cross-sectional area of the porous medium. The intrinsic permeability (k) roughly estimated using the Kozeny–Carman relation fell within the range of $1.09 \times 10^{-11} \leq k \leq 2.75 \times 10^{-10}$ m^2. In most geological formations of CO_2 sequestration, the particle sizes and porosity values for highly porous and permeable sedimentary typically vary from 60 μm to 2000 μm and 0.2 to 0.3, respectively (Carbillet et al., 2022; Payton et al., 2020; Nelson., 2004), indicating that the choice of porous media used in the present study can also represent the real porous media for CO_2 sequestration.

2.2. Fluid pairs

Table 1 lists the fluid pairs used in the single- and two-phase flow experiments and their physical properties. In the context of CO_2 injection in the NBZ, the two-phase flow displacement between supercritical liquid CO_2 and brine at low temperature and high pressure does not induce slippage due to the absence of a gaseous phase. Therefore, water and silicone oil were used to model liquid CO_2 and brine as invading and defending liquids, respectively, in the two-phase flow experiments. The choice of using water to model the CO_2 injection in NBZ-CCS is also to neglect the CO_2 dissolution effect and to handle laboratory experiments easily, as utilizing the supercritical CO_2 in flooding experiments requires high-pressure setup systems. To observe the invading water flow in the pipe or at the breakthrough time, the water was colored by adding 1 wt.% of blue food coloring to the mixture. However, 5 wt.% of 1-iodododecane was added to the silicon oil (10 cS) because of its high X-ray attenuation, enabling the identification of its contrast compared with the other phases. For the drainage process, a non-wetting phase (NWP) is injected into the porous medium saturated by WP. The displacement of the saturated NWP in porous media by the injected WP is referred to as an imbibition process. In most rock reservoirs, brine displacement via injected CO_2 is a drainage process (Yang et al., 2019). It should be noted that the wettability of porous media determines the nature of the IP or DP. The viscosity and density of the fluids and interfacial tension were measured at 22 °C. We estimated the bond number (Bo) to determine whether or not the buoyancy effect exists during fluid–fluid displacement. Bo is the ratio between the gravitational and interfacial tension forces. $Bo = \Delta\rho g L^2/\gamma$, where $\Delta\rho$ is the difference between the densities of water (ρ_w) and silicon oil (ρ_o) ($\Delta\rho = \rho_w - \rho_o$), g is the gravity, and L is the characteristic pore size (200–1000 μm). Thus, the estimated Bo ranges between 7.07×10^{-4} and 1.77×10^{-2}, showing that the buoyancy effect was attributed to the fluids and particles displacement in this study (Muharrik et al., 2018).

Table 1
Physical properties of the fluids.

Exp.	Fluids pairs	Type	Viscosity, μ[a] (m · Pas)	Density, ρ[b] (kg/m^3)	Interfacial tension, γ[c] (mN/m)
Drainage	Silicon oil (10 cS) + 5 wt.% 1-iodododecane	WP (DP)	8.4	935	34.4
	Water + 1 wt.% blue food coloring	NWP (IP)	1.14	997	-
Imbibition	Silicon oil (10 cS) + 5 wt.% 1-iodododecane	NWP (DP)	8.4	935	34.4
	Water + 1 wt.% blue food coloring	WP (IP)	1.14	997	-
Single-phase flow	Pure water	WP	1.0	997	-
	Water + 1 wt.% blue food coloring	WP	1.14	997	-

[a] Viscosity was measured using a tuning fork viscometer at 22 °C (A & D Co., Ltd., SV 10).
[b] Density was measured using a hydrometer at 22 °C.
[c] Interfacial tension was measured using a drop shape analyzer at 0.1 MPa and 22 °C (DAS25S).

2.3. Experimental procedures

The experimental procedures included four important steps: Steps 1–4 include the packed bed preparation; initial saturation and scan; invading fluid injection; and final scan and reconstruction of CT images, respectively. The detailed procedures of each step are as follows.

Step 1: The inner cylinder tube was initially painted with vacuum grease at a height of 20 mm. We filled the fine beads ($d_s = 200$ μm), which had water-wet and oil-wet surfaces near the inner wall of the tube for single- and two-phase flow experiments. Since tiny particles are easily attached to the grease on the inner wall, a small permeable layer (<0.5 mm) was created to prevent a wall effect where the invading fluid preferentially flowed throughout the tube wall. The moist-tamping method (Ladd, 1978) was employed with a few drops of defending fluid on the particle mixture to minimize the segregation of both grain sizes. Finally, we gradually filled the packed bed with the particle mixture with gentle vibration to achieve a random and uniform packing.

Step 2: Immediately after the packed bed was prepared, it was submerged in a container filled with defending fluid and placed in a vacuum chamber for approximately 1 h. This method enabled us to complete the initial saturation of the porous medium. The detailed description of this method is described by Patmonoaji et al. (2020a). An X-ray CT scanner (Comscantechno, ScanXmate-CF110TSS300) was used to investigate particle migration by fluid–particle interactions for single- and two-phase flow experiments. The prepared sample was vertically placed between the X-ray source and detector in the X-ray CT scanner (Fig. 1(A)) for the initial scan to confirm that the porous medium was perfectly saturated with the defending fluid and no trapped air or bubbles were inside. Here, two full scans of the top and bottom parts were conducted to cover the entire packed bed (Fig. 1(A)). Each full scan produced 1300 images with 2400 projections at 1.0 frame per second during a 360° rotation of the packed bed, and the complete scan took 40 mins. The intensity of the X-ray source for each scan remained the same under all experimental conditions (90 kV, voltage; 120 μA, current). The pixel size was set to 8.489 μm/pixel. Comparing the pixel size of the X-ray and the average diameter of the fine and grain particles, the spatial resolution roughly corresponded to $23.6d_s$ and $117.8d_l$, respectively. This was sufficiently accurate to visualize or trace the particle migration in the medium during fluid injection (Fig. 2).

Step 3. After the initial scan, the invading fluid was upwardly injected using a syringe pump (KD Scientific Gemini 88 Plus). For strong drainage and single-phase flow experiments, 0.1 and 0.2 pore volumes (PV) were injected into the packed bed to investigate the suffusion or fine migration by fluid–fluid and fluid–particle interactions. Except in the case of strong imbibition, the injected PV was increased to 0.12 or 0.14 PV at $Q = 10$ and 50 mL/hr, respectively, after 0.3 PV was injected. Table 2 summarizes the experimental conditions for each experiment. The key parameters that were used to simulate or refer to the conditions of CO_2 sequestration were LogCa and Log$M$. Here, for strong drainage and imbibition, Q was varied within the range of 0.1 mL/$h \leq Q \leq$ 50 mL/h, corresponding to a LogCa range of $-7.476 \leq \text{Log}Ca \leq -4.777$, whereas the viscosity ratio was fixed (Log$M = -0.867$). These conditions were closely located in the transition of the CF to VF in the immiscible two-phase flow displacement diagram (Fig. 1S). However, for single-phase flow experiments, the Q range was 1 mL/$h \leq Q \leq$ 50 mL/h. The Reynolds number, $Re = \rho_w v d_s/\mu_{IP}$, range $1.76 \times 10^{-4} \leq Re \leq 8.81 \times 10^{-2}$, indicating that each experiment was performed in a Darcy regime ($Re < 10$); thus, the inertia force was negligible. The injection was stopped until a breakthrough was observed. The breakthrough was confirmed, and the experiment ended when the most advancing doped water or IP reached the wire–mesh, as evidenced by the reconstructed X-ray CT images. Consequently, only a minimal IP amount accumulated between the wire–mesh and the outlet, which does not affect particle migration. In the present work, we investigated particle migration by fluid–particle interactions when the system was purely governed by competition between capillary or interfacial tension and viscous forces, which was before the breakthrough. After the breakthrough, the fluid–fluid displacement spanned the system and lowered the pressure gradient, maintained constant fluid–particle shear, and left the interface unchanged. Therefore, particle migration is not significant after the breakthrough. Immediately after each IP injection amount, fluids and particles may redistribute due to residual pressure, particularly at high flow rates, causing scans at quasi-equilibrium and affecting CT image quality. Therefore, we waited about 5 min before scanning the packed bed to ensure full stability. Hu et al. (2020) referred to this process as a discontinuous injection method, where a small amount of invading fluid was injected and then stopped and scanned. Owing to the limitations of our X-ray CT's static mode, we could not perform continuous injection during the displacement, as capturing 3D images at breakthrough was difficult. The scanning required twice (bottom and top) to cover the entire packed bed, with each scan requiring 40 mins.

Step 4. The reconstructed images of each full scan comprised 1300 × 1300 × 1300 voxels in all directions, corresponding to 11.03 × 11.03 × 11.03 mm^3. During the reconstruction, filters, such as noise, ring artifacts, and beam hardening reduction, mounted in the reconstructed software (coneCTexpress) were applied to smooth the obtained X-ray raw grayscale images (16 bits) before further processing them using ImageJ. Next, we present the image-processing

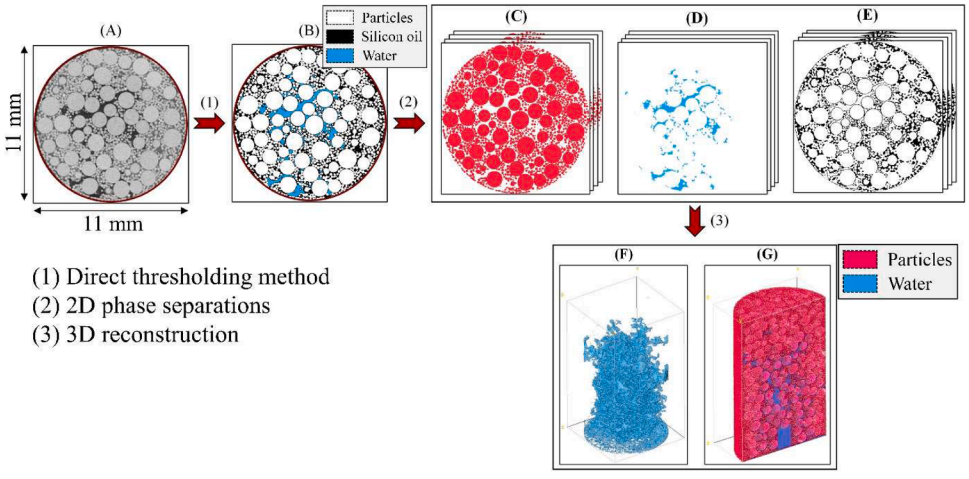

Fig. 2. Workflow of image-processing techniques. (A) X-ray CT images after filtering (the brightest is the glass beads or particles, whereas the darkest or black is the water or invading phase; between them is silicon oil or the defending phase). (B) Binary image of combined phases via direct thresholding, (C) particle phase, (D) water phase, (E) silicon oil phase. Three-dimensional (3D) reconstruction of (F) water phase and (G) 3D cross-sectional view of injected fluid–particle interactions.

Table 2
Experimental conditions.

Exp.	Wettability	Flow rate, Q [mL/h]	Characteristic velocity, v [mm/s]	Capillary number, LogCa [−]	Reynolds number, Re [−]	Viscosity ratio, Log$M$ [−]
Drainage	Strong oil-wet	0.1	0.001	−7.476	1.76×10^{-4}	−0.867
		1	0.010	−6.476	1.76×10^{-3}	
		10	0.101	−5.476	1.76×10^{-2}	
		50	0.504	−4.777	8.81×10^{-2}	
Imbibition	Strong water-wet	0.1	0.001	−7.476	1.76×10^{-4}	−0.867
		1	0.010	−6.476	1.76×10^{-3}	
		10	0.101	−5.476	1.76×10^{-2}	
		50	0.504	−4.777	8.81×10^{-2}	
Single-phase flow	Strong water-wet	1	0.010	-	1.76×10^{-3}	0.057
		10	0.101	-	1.76×10^{-2}	
		50	0.504	-	8.81×10^{-2}	

procedures for the qualitative visualizations of 2D and 3D images using ImageJ.

2.4. Image processing

Image-processing software (ImageJ) was employed to visualize the 2D and 3D images of fluid–fluid displacement and particle migration in the porous medium. Fig. 2 shows the workflow of the image-processing techniques.

The images from each scan were initially realigned in the horizontal and vertical directions. Each horizontal cross-sectional image was centered before cropping. The cropped horizontal cross-sectional area was 11.0 × 11.0 mm^2 (Fig. 2(A)). Each top and bottom scan of the packed bed consisted of 1300 image slices. Owing to the cone-beam scanning effect of the X-ray CT, where image quality near the top and bottom regions is low, we discarded 125 and 75 slices from the top and bottom regions of the top scan and 75 and 100 slices from the top and bottom regions of the bottom scan. After removing and aligning the images, 2227 images remained, corresponding to 18.91 mm^3. Thus, the entire 3D volume of the combined images for the visualization of fluid–fluid displacement and particle migration was 11.0 × 11.0 × 18.91 mm^3.

Prior to binarization, the raw images from the X-ray CT were filtered to remove noise using “remove outliers” and “median filter” in ImageJ, indicating a clear difference between water, silicon oil, and glass bead particles (Fig. 2(A)). Direct thresholding (Alhammadi et al., 2020; Patmonoaji et al., 2020a; She et al., 2022) with an automated threshold value based on the image contrast was applied to separate the particle and fluid phases (Fig. 2(B)). Thereafter, the separated phase images were converted into binary images (8 bits) (Fig. 2(C–E)). The watershed segmentation algorithm (Patmonoaji et al., 2020b; Rabbani et al., 2016) defined the individual pores and particles between the large and small particles from the 2D horizontal images. The segmentation of each phase is highly accurate depending on the X-ray CT or image resolution (Andrew et al., 2015; Hu et al., 2020; Patmonoaji et al., 2020b; Peng et al., 2012; Rabbani et al., 2016). In our experiments, the X-ray CT is high enough to accurately segment the particle and fluids phase, as shown in Fig. 2. However, it is challenging to clearly observe the thin film (≈ 1μm) (Krummel et al., 2012) between small particles when they aggregated or are stick to each other during the flow. To reconstruct the 3D structure of the invading phase and fluid–particle interactions in the porous media (Fig. 2(F–G)), the volume viewer in ImageJ was applied to the stack images of each phase and combined phases (Fig. 2(B–E)). To trace the particle movement for each invading fluid injection, the images before each injection were subtracted from the images after each injection consecutively using the “image calculator” in ImageJ.

Finally, based on the binarized images of the particle and fluid phases, we roughly estimated various parameters, such as porosity, packing density of particles, and invading fluid saturation. During the fluid injection and packing process with vibration, fine particles may accumulate at the top (near the wire mesh) and bottom regions. To neglect this effect, the region of interest for evaluating these parameters was 11.0 × 11.0 × 16 mm^3, which implies that approximately 1.45 mm of the top and bottom images were excluded. The pore fraction from each horizontal cross-sectional area image was used to estimate the porosity (ϕ) of both porous media (Fig. 1(B)). The saturation of the IP was calculated using the ratio of the IP to the pore fraction corresponding to each injected PV.

3. Results and discussion

3.1. Drainage system

3.1.1. Displacement structure of invading phase and saturation

Fig. 3 shows the development of the 3D structure of the IP and its saturation with the injection PV at various flow rates. The transition of the invading fluid structure can be observed with an increase in the flow rate Q (left bottom to top). At a low flow rate ($Q = 0.1$ mL/h) (Fig. 3(A)), immediately after injecting 0.1 PV, the IP rapidly invaded forward and spread in various directions, even in the backward direction from the injection point, forming a structure-like finger with several branches or clusters. With the addition of the injection volume to 0.2 PV, the IP further advanced by following the preferential flow paths along the injection direction, increasing the individual cluster size or finger width. At 0.3 PV, as the IP continued to develop in every direction, its structure became compact, resembling CF characteristics. At 0.4 PV, the breakthrough was observed, and the IP structure became more compact or concentrated. At $Q = 1$ mL/h (Fig. 3(B)), similar to the case of $Q = 0.1$ mL/h, the IP structure rapidly formed after the injection. However, the growth of the IP structure with the injection volume significantly differed from that observed in the case of $Q = 0.1$ mL/h. The IP tended to rapidly develop forward with just a few thin fingers, resembling VF characteristics. In two-phase flow displacement, with an increase in Q or LogCa, the viscous force enhances its strength over the capillary force. This results in a faster displacement of the invading fluid in the mean flow direction because of the enhancement of the pressure gradient in the medium. Thus, the invading fluid exhibited a streak-like structure or VF (Lenormand et al., 1988), and breakthrough occurred earlier. At $Q = 10$ mL/h (Fig. 3(C)), the IP preferentially extended along the central axis of the packed bed and continued progressing to the outlet. The finger volume was smaller compared with that at lower Q values. For $Q = 50$ mL/h (Fig. 3(D)), the IP aggressively developed vertically, exhibiting the streak-like structure with the fingertip reaching the outlet at 0.1 PV, as the viscous forces dominated the capillary forces. The transition of the displacement pattern from a compact structure to a streak-like structure with an increase in Q or LogCa for drainage has been discussed by Zhao et al. (2016).

The IP or NWP saturation profiles corresponding to each Q value are shown in Fig. 3 (right panels). The distance from the inlet was normalized by the height of the packed bed (z/H). The initial saturation was approximately 0.1 because only a small portion of the IP was in the nozzle before the injection (0 PV). The IP saturation increased with the

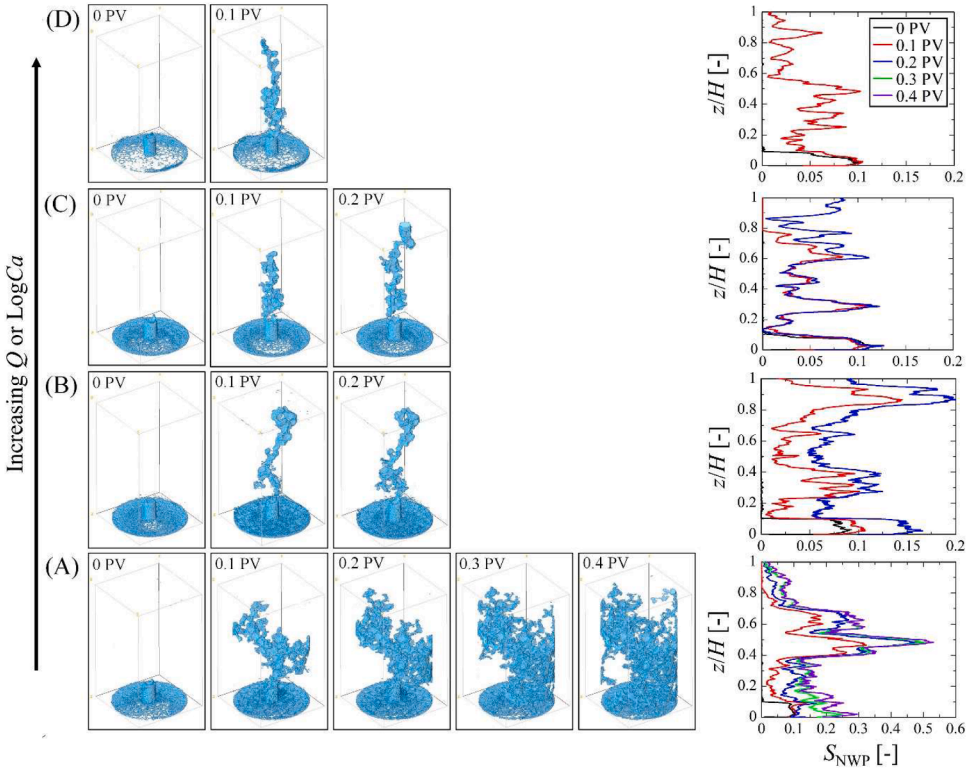

Fig. 3. Development of the 3D structure of invading fluid after injecting every 0.1 PV into the packed bed at (A) 0.1, (B) 1, (C) 10, and (D) 50 mL/h (left panels). Q (flow rate) or LogCa increases from the bottom to the top (black arrow). The panels on the right show the saturation profiles of the invading NWP.

injection amount at all Q values and was larger at the front than that at the top after the breakthrough. The invading fluid exhibited unstable propagations along the flow directions because of the migration of fine particles. The IP saturation at a low Q (0.1 mL/h) (Fig. 3(A)) significantly increased to approximately 0.55 ($z/H = 0.4$–0.6) at breakthrough time. The drastic increase in saturation value was attributed to a greater interface expansion. When the NWP invades and displaces the particles, the interface between the two phases will easily and locally expand in that region. At a large Q (50 mL/h), the saturation remained low ($S_{NWP} < 0.12$) along the packed bed, reflecting the streak-like structure or VF (Fig. 3(D)). The average saturation of the IP at breakthrough decreased from 0.188 to 0.044 with an increase in Q or LogCa (Fig. 2S). The decreasing saturation or displacement efficiency with an increase in Q or LogCa reflects the transition of CF to VF at Log$M < 0$, consistent with previous studies (Chen et al., 2017; Han et al., 2020; Islam et al., 2014; Lenormand et al., 1988; Zhao et al., 2016). The displacement efficiency or invading fluid saturation in heterogeneous porous media was lower than that in homogeneous media because the heterogeneity during the injection process diminished the displacement stability (Liu et al., 2015).

3.1.2. *Invasion front behavior of invading phase*

Fig. 4 illustrates the displacement behavior of the NWP with the injection PV at various Q values in the case of drainage. After the NWP injection into the WP-saturated medium, the invasion front of the NWP was established, and the interface between the NWP and WP became unstable. The NWP invaded the large pores selectively due to lower capillary pressure. At a low Q (0.1 mL/h) (Fig. 4(A)), the interface between the NWP and WP expanded with a continuous increase in the injection PV (red circles), inducing particle displacement in all directions and a sudden increase in the NWP saturation. In other words, the interfacial area between the two phases was increased during the interface expansion process, potentially changing the medium properties and fluid flow characteristics. Fig. 3S shows the interface expansion during fluid–fluid displacement at $Q = 0.1$ mL/h. A similar behavior of interface expansion near the invasion front was also observed at $Q = 1$ mL/h. The interface expansion gradually reduced with an increase in Q (Fig. 4(C-D)) as the viscous force dominated the capillary force. Thus, the invading NWP vertically extended forward to the outlet. The evolution of displacement with injection volume was not observed in the case of $Q = 50$ mL/h, as the breakthrough occurred considerably earlier than in other Q cases.

Interface expansion was observed near the invasion front of NWP at $Q = 1$ mL/h (Fig. 4(E)). After injecting 0.1 PV, the invasion front of the NWP bypassed the pores and left a large amount of the WP in the front, generating structure-like fingers. As the injection volume increased to 0.2 PV, the finger or cluster volume increased because of faster coalescence between the neighboring fingers, indicating interface expansion during fluid–fluid displacement. This characteristic is similar to the Haines jump event, which often occurs at a low Q or LogCa at an extremely rapid timescale. However, owing to the limitations of our X-ray CT, we could not show the rapid evolution of the injected fluid or the Haines jump event with continuous injection. High-performance X-ray CT or a supercomputer is required to qualitatively capture or simulate the Haines jump process in 3D or 4D porous media (Berg et al., 2013; Cooper et al., 2017; Moebius and Or, 2012; Tekseth et al., 2023; Wang et al., 2024). When the interface between the two phases continuously expands, the fluid–particle interaction is enhanced, resulting in a greater particle migration in the medium. Hu et al. (2020) studied 3D drainage displacement in homogeneous porous media, where particle migration was absent, under varying Ca and M conditions. They found that the fluid-fluid displacement shifted from CF to VF under high Ca and low M, which also aligned with current results. However, the invasion behavior of the IP differs when particle migration is present due to fluid-particle interaction and pressure fluctuation, which will be discussed later. With particle migration, the IP invasion front is non-uniform due to fluid-particle interaction that expands the interface between the two fluids and fluctuating pressure distribution. In contrast, the IP front

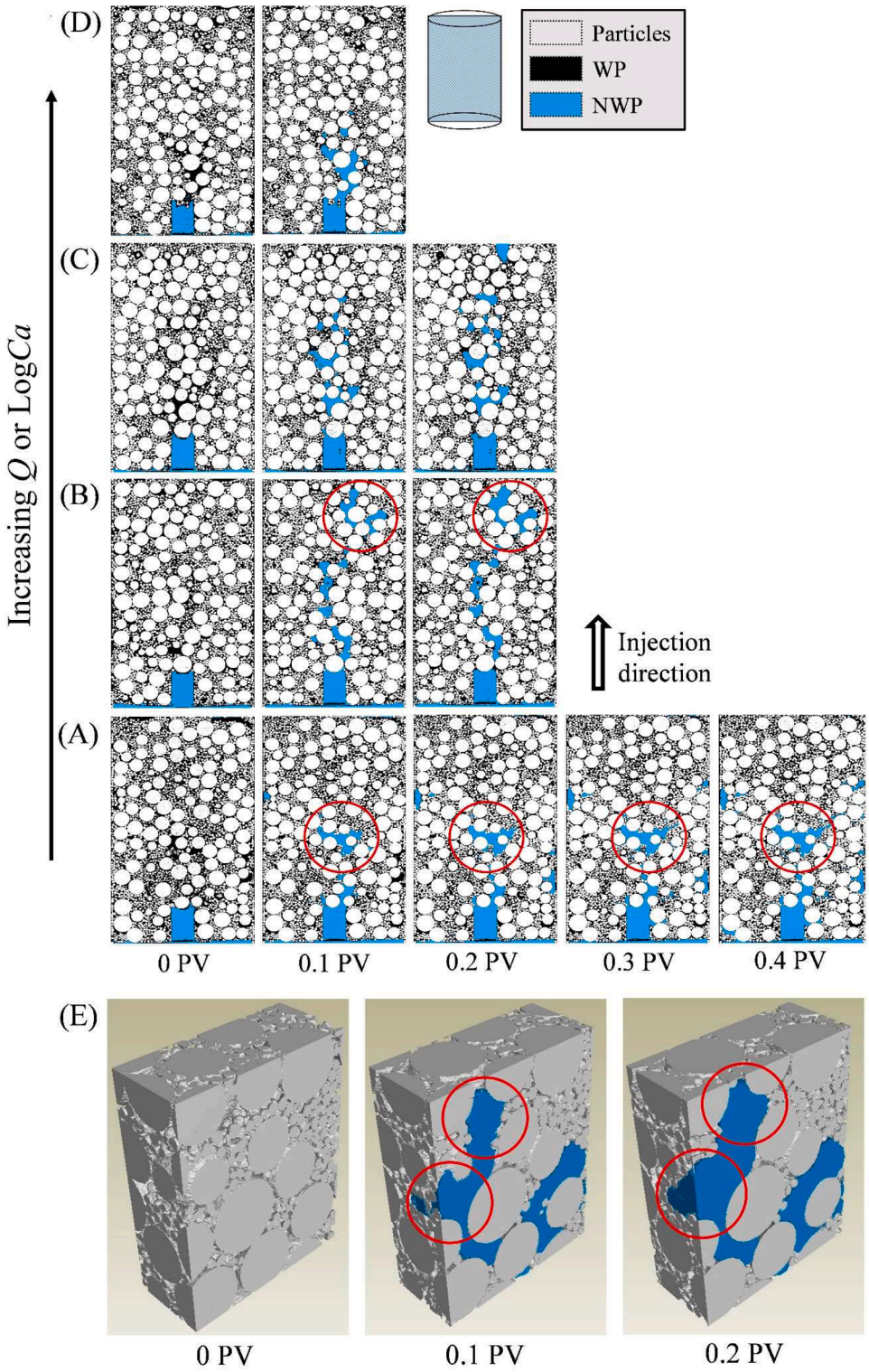

Fig. 4. Vertical cross-sectional images of invading fluid or NWP after injecting 0.1 PV into the packed bed at (A) 0.1, (B) 1, (C) 10, and (D) 50 mL/h (top panels). The white, blue, and black colors denote the particle, NWP, and WP, respectively. The horizontal cross-sectional images of fluid–fluid and fluid–particle interactions at all Q values are shown in Figs. 3S–6S. The bottom panels show the 3D cross-sectional views of the invasion front behavior of the IP at (E) $Q = 1$ mL/h, randomly taken near the front with a region of interest of $1.07 \times 3.92 \times 4.24$ mm^3. The gray and blue colors denote the particle phase and IP, whereas the empty pore represents the defending phase (DP). The region marked with red circles indicates the interface expansion between the IP and DP.

remains stable without particle migration, as the fluid-particle interface remains unchanged.

3.1.3. Effects of interfacial tension and viscous force on particle migration

This section discusses the combined effects of interfacial tension and viscous force on particle migration for drainage displacement. The experimental results of single-phase flow were used as a reference system.

Fig. 5 illustrates the migration of particles with injection PV at varying flow rates for drainage and single-phase flow experiments. For

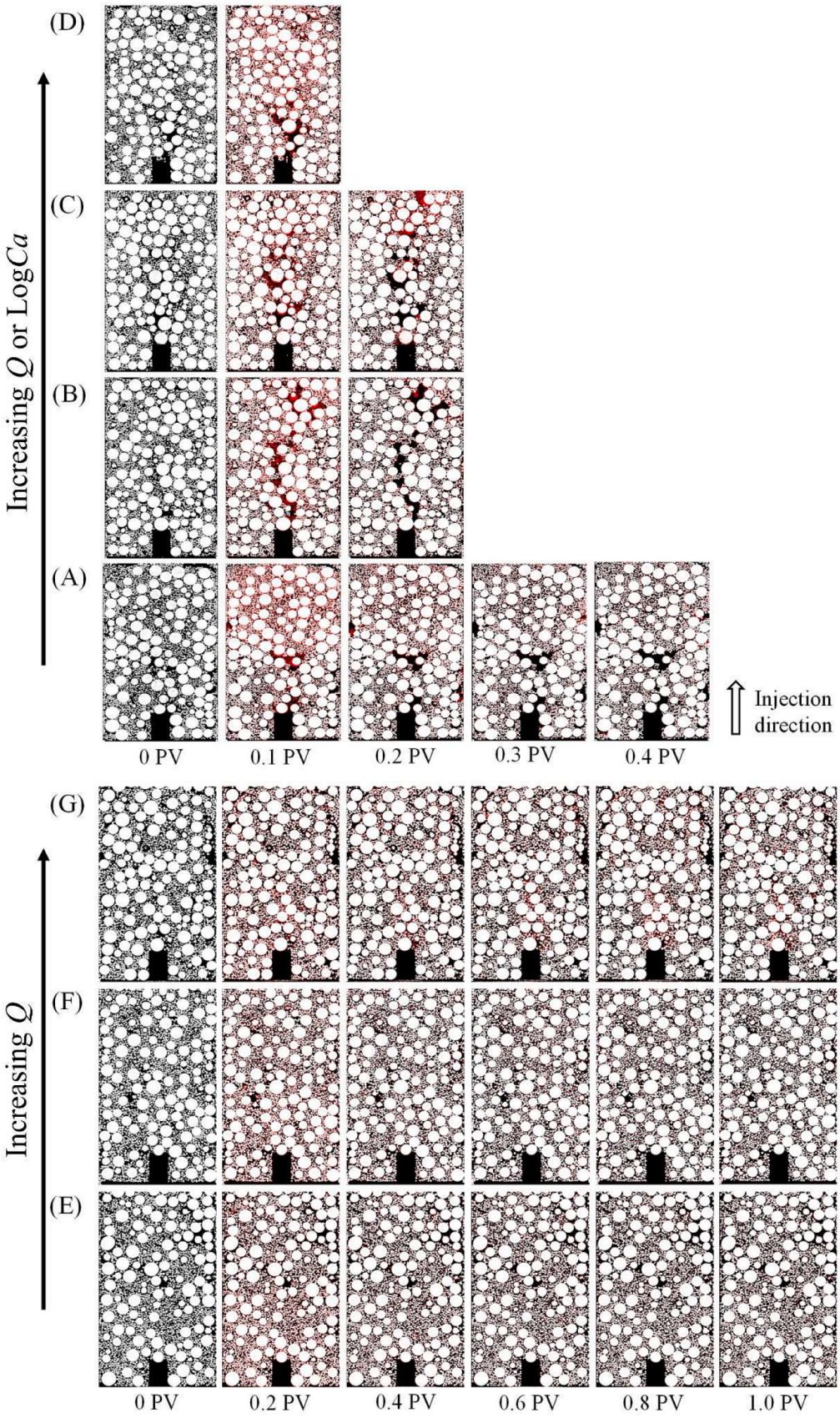

Fig. 5. Vertical cross-sectional images of particle migration with injection pore volume for drainage displacement at various Q values (A) 0.1, (B) 1, (C) 10, and (D) 50 mL/h (top panels) and single-phase flow at (E) 1, (F) 10, and (G) 50 mL/h (bottom panels). The red color denotes the particle movement compared with that in the previous scan after each injection. The horizontal cross-sectional images of particle migration for strong drainage and single-phase flow experiments at all Q values are shown in Figs. 7S –13S.

strong drainage (Fig. 5, top panels), at a low Q (0.1 mL/h) (Fig. 5(A)), after the injection of 0.1 PV, the particles were displaced throughout the medium as the NWP invasion propagated in various directions (Fig. 4 (A)). Particles continued to migrate with an increase in the NWP injection volume. The interplay between interfacial tension and pore structure heterogeneity caused localized particles accumulation or pore-clogging in certain regions. However, the particle movement was less significant than the first injection or invasion front due to preferential flows. As discussed above, at a low Q or LogCa, interfacial tension dominated the viscous force, promoting interface expansion between the NWP and WP. Thus, particle migration significantly proceeded in all directions, altering the pore networks of the entire medium (Fig. 5(A)). The moving or expansionary interface promotes in-situ particle migration, or remobilization was also observed in immiscible gas-water systems (Han et al., 2018; Huang et al., 2018; Jung et al., 2018). As the Q or LogCa increased, the viscous force was gradually enhanced and paired with the interfacial tension when displacing the particles for each injection. At $Q = 1$ mL/h (Fig. 5(B)), the particle migration tended to be more significant, as fine particles were further displaced with the NWP invasion. A similar behavior was observed at $Q = 10$ mL/h. At large Q values (10 mL/h and 50 mL/h), the fluid–particle interactions were strongly enhanced owing to higher shear forces, leading to a greater particle displacement throughout the medium (Figs. 5(C&D)).

To elucidate the interfacial tension effect on particle migration in two-phase flow experiments, we conducted additional single-phase flow experiments for comparison (Fig. 5, bottom panels). The displacement of particles while varying the flow rate and injection PV was not strong compared with the drainage displacement. In single-phase flow, viscous or drag force is the only pronounced effect governing particle migration, with no interfacial tension. Critical flow rate (Q_c) is the threshold value at which the flow is adequately strong to displace particles from the pore structure and initiate internal erosion by suffusion. We roughly estimated the Q_c using the same particle ratio between small and large particles and the same packed bed. As a result, Q_c was approximately 140.42 mL/h in our system. Particle movement just slightly proceeds near the injection point (Figs. 5(E–G)) because the utilized flow rates were lower than the Q_c, consistent with Nguyen et al. (2019), who reported that particle migration was insignificant under continuous seepage flows if the inflow rate into the medium was below the Q_c. Comparing the particle migration in the medium at the same flow rate ($Q = 1$ mL/h) in drainage (Fig. 5(B)) and single-phase flow experiments (Fig. 5(E)), interfacial tension significantly impacted particle migration in an immiscible two-phase displacement process, clearly indicating the effect of two-phase flow on particle migration compared with single-phase flow. In the current single-phase flow experiments, the injected water has a higher viscosity than the water-saturated porous media, creating a viscosity contrast that reduces the inflow rate and pressure gradient, limiting particle migration. However, when the

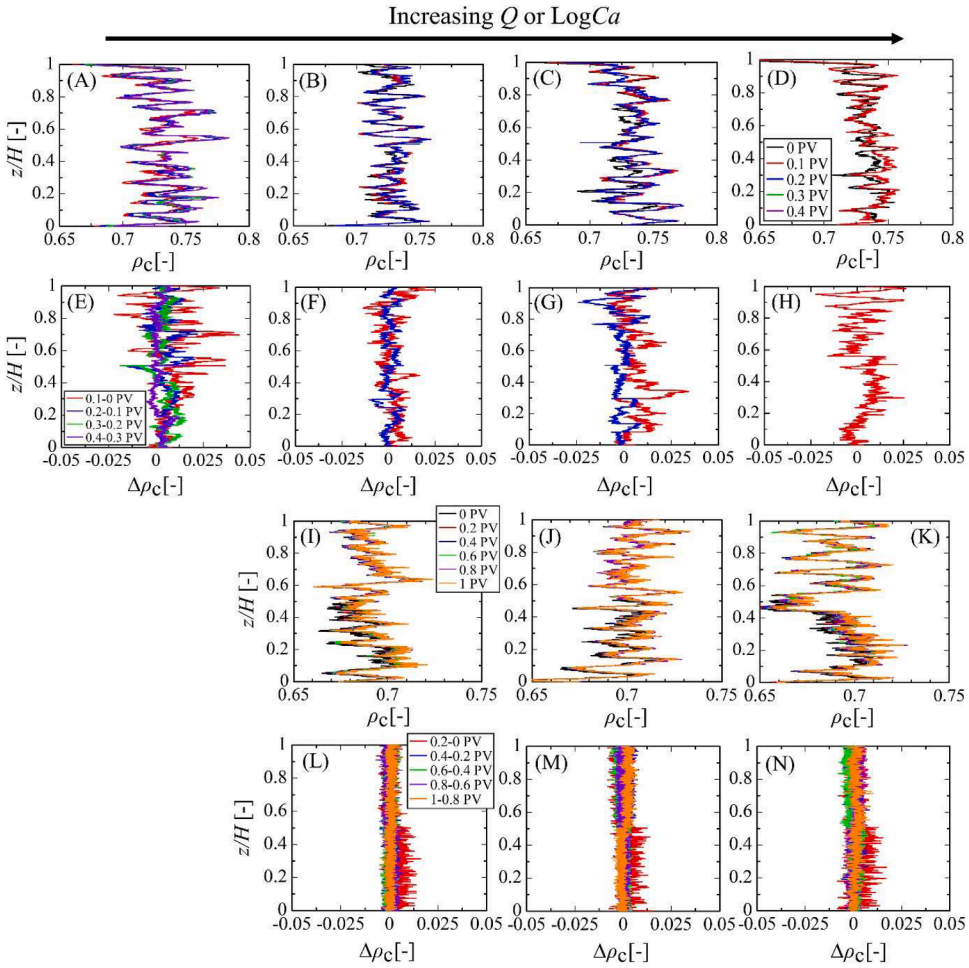

Fig. 6. Vertical profiles of ρ_c and $\Delta\rho_c$ along the packed bed. The top panels show the distribution of the ρ_c of particles along the packed bed at various Q values (A) 0.1, (B) 1, (C) 10, and (D) 50 mL/h (top first row) and $\Delta\rho_c$ for each injection volume of the invading phase (IP) at (E) 0.1, (F) 1, (G) 10, and (H) 50 mL/h (top second row) in drainage displacement. The bottom panels show the distribution of the ρ_c of particles along the packed bed at various Q values (I) 1, (J) 10, and (K) 50 mL/h (bottom first row) and the $\Delta\rho_c$ for each injection volume of the IP at (L) 1, (M) 10, (N) 50 mL/h (bottom second row) in single-phase flow experiments. Q (flow rate) or LogCa increases from left to right (black arrow).

viscosities match, the pressure gradient is evenly distributed, promoting particle migration (Prasomsri and Takahashi, 2021).

3.1.4. Packing density profile

The particle migration with injection volume at different Q values for drainage and singlephase flow experiments were visualized to understand the effects of interfacial tension and viscous force in the system (Fig. 5). Fig. 6 shows the packing density (ρ_c)($\rho_c = 1 - \phi$) of the particles and the change in packing density ($\Delta\rho_c$) for each injection at various Q values. The packing density profile or value (at 0 PV) slightly differed for each Q condition because of the different constriction or segregation between small and large particles during the packing process with the moist-tamping method. As shown in Fig. 5 (first and third rows), the measured ρ_c for all Q values fell within the range of $0.7 - 0.775$. Only a slight change in ρ_c in the vertical distribution was observed with an increase in the injection PV. We estimated the $\Delta\rho_c$ for each injection flow rate to understand the migration mechanism of the particles in the medium. The $\Delta\rho_c$ was defined as $\Delta\rho_c = \rho_{Cn+1} - \rho_{cn}$, where ρ_{cn+1} and ρ_{cn} are the packing densities after and before each injection volume, respectively. The positive increase in $\Delta\rho_c$ after each injection indicates particle displacement from the low to high regions. The greater the packing density, the lower the porosity of the medium. Contrarily, the negative value might have been caused by the fall of particles due to gravity, as the particle density exceeds that of the defending fluid, and the backward movement of particles due to the invasion of the injected fluid (Fig. 4). At the same Q values, in the drainage case (Figs. 6(F–H)), particle migration occurred in the entire medium while it slightly progressed near the injection point during single-phase flow experiments (Figs. 6(L–N)), reflecting the vertical images shown in Fig. 5. The effect of the interfacial tension is a major factor that causes a difference in particle migration in two-phase and single-phase flow experiments, as discussed above.

3.2. Imbibition system

3.2.1. Displacement structure of invading phase and saturation

Fig. 7 shows the development of the 3D structure of the IP and its saturation profile with the injection PV at various flow rates. The transition of the invading fluid structure significantly differed from that in the strong drainage case (Fig. 3). The IP structure shifts from a streak-like structure to a compact structure with an increase in Q or LogCa (Figs. 7(A–D)). At a low Q (0.1 mL/h) (Fig. 7(A)), the IP tended to develop forward along the vertical direction, forming a streak-like structure after 0.1 PV was injected into the packed bed. The IP was continually displaced toward the preferential flow paths, reaching the outlet at 0.2 PV. At $Q = 1$ mL/h, the IP propagated in all directions, even backward, as the capillary entrance pressure increased (Herring et al., 2017), leading to a compact structure with small connected clusters. At $Q = 10$ mL/h (Fig. 7(C)), the IP structure became more compact or concentrated, reaching the outlet at 0.54 PV. A similar structure was observed at $Q = 50$ mL/h (Fig. 7(D)). At high flow rates, the capillary pressure become weak, as the capillary shifted to viscous flow, allowing the IP to penetrate smaller pores more easily. The invading fluid structure typically changes from compact to burst-like structures with an increase in Q, whether the displacement is drainage or imbibition, as the viscous force gradually dominates the capillary force (Hu et al., 2020; Patmonoaji et al., 2020a; Yang et al., 2019; Zhao et al., 2016). However, the wettability of the porous media influenced the invading fluid structure. Zhao et al. (2016) studied the wettability control on immiscible fluid–fluid displacement patterns in 2D synthetic microfluidics. The displacement became less efficient with an increase in Ca or LogCa, except for strong imbibition, as observed in the present 3D heterogeneous porous media study.

The saturation profiles of the WP corresponding to each Q are shown in Fig. 7 (right panels). As the invading WP rapidly propagated in all directions, the bulk of the WP was observed near the injection point, resulting in higher saturation near the front region than that near the outlet region. The saturation of the invading WP increased with the injection PV at all Q values, reflecting the 3D structure of the invading

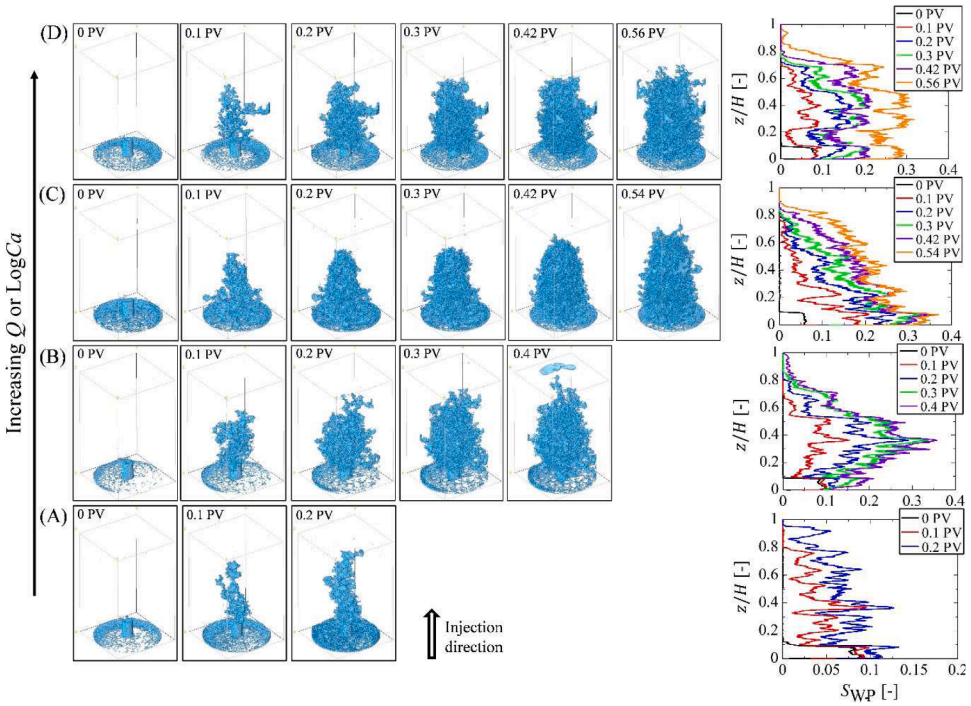

Fig. 7. Development of the 3D structure of invading fluid after injecting every 0.1 PV into the packed bed at (A) 0.1, (B) 1, (C) 10, and (D) 50 mL/h (left panels). Q (flow rate) or LogCa increases from the bottom to the top (black arrow). The panels on the right show the saturation profiles of the invading WP.

fluid (Figs. 7(A–D)). As Q or LogCa increased, the average saturation of the IP at breakthrough increased from 0.06 to 0.19 (Fig. 14S), opposite that of the strong drainage case. The main factors causing this discrepancy were the capillarity and spontaneous displacement between the strong imbibition and drainage. In strong imbibition, the smallest pore spaces are spontaneously invaded as their surfaces have a higher affinity for the WP. This results in a uniform spread of the invading WP, which overcomes the capillary resistance and increases the WP saturation through the medium as LogCa increases. However, in strong drainage, as explained above, the NWP invasion followed the preferential flow through the larger pores at larger LogCa values, leaving a large amount of the WP in between the invasion front because the higher capillary resistance in the smaller pores (Figs. 3 and 4).

3.2.2. Invasion front behavior of invading phase

Fig. 8 illustrates the displacement behavior of WP with the injection PV at various Q values. The invading WP spread in all directions while penetrating small and large pores and preferentially wet the particle surfaces at all Q values (Figs. 8(A–D)). At a low Q (0.1 mL/h), after the WP injection, the WP tended to slowly displace the NWP from the pore spaces while fines migration may have also proceeded. The WP continued progressing forward, following the opened channels as the injection amount increased, although the capillary force increased at a low Q or LogCa. This was because of film or corner flows influenced by the wettability of the medium (strong water-wet). The strong affinity or surface roughness of the hydrophilic or strong water-wet medium for the injected WP enhanced the WP displacement, following the created flow directions. At a high Q (50 mL/h), the WP further spread in all directions and significantly displaced the NWP, as the invading WP perfectly wetted the particle surfaces, leaving the NWP in the pore bodies and producing the film or corner flows in the system. This phenomenon was observed in 2D experiments in the flow cells for strong or forced imbibition by Zhao et al. (2016) and Levaché and Bartolo (2014) and was predicted in strong water-wet 3D porous media (Constantinides and Payatakes, 2000; Idowu and Blunt, 2010; Patzek, 2001). In 3D heterogeneous porous media, the strongly interconnected pores between coarse- and fine-grained sediments may have also contributed to the film or corner flow because of the higher capillary pressure in the fine-grained regions. The higher capillary pressure in interconnected pores enhances the spontaneous displacement of the WP to the edges in the smaller pores, producing film or corner flow along the grain surfaces. Thus, the film formation in the system reduced the significance of the interfacial tension effect between the WP and NWP at the interface and produced a uniform pressure distribution in the medium compared with the strong drainage case. As a result, the WP displaced the particles in its invasion direction with an increase in the injected amount (Fig. 8(E)).

3.2.3. Effects of interfacial tension and viscous force on particle migration

Fig. 9 illustrates the particle migration with the injection PV at various Q values in imbibition displacement. As the injection volume increased, fine particles migrated with the WP invasion while large particles remained in their initial position throughout the medium at all flow rates (Fig. 9(A-D)). With an increase in Q or LogCa, the fine particles further migrated as the WP invaded small and large pores and then spread in all directions (Figs. 8(A–D)). However, compared with strong drainage, particle displacement tended to be less significant in strong imbibition. When the film formation surrounded a particle, it created a shield for the particle and stabilized the interface, reducing the shear forces acting on the fluid–particle interactions and the effect of interfacial tension between the two phases.

3.2.4. Packing density profile

Fig. 10 shows the ρ_c of the particles and the $\Delta\rho_c$ for each injection at various Q values. Similar to drainage (Figs. 5(A–D), top panels), particle migration proceeded throughout the medium with the injection volume at all flow rates (Figs. 9(A–D)). However, the increase in $\Delta\rho_c$ indicating particle movement from the low to the high region was not larger, and the $\Delta\rho_c$ was gentle compared with the drainage case at all Q values (Fig. 6, top panels). This suggested that the particle migration for strong imbibition displacement was less significant owing to the reduction of the interfacial tension effect by film formations.

3.3. Injection pressure

An understanding of the injection pressure in fluid–fluid displacement and fluid–particle interactions is crucial for geological applications. Thus, we conducted supplementary pressure measurement experiments during continuous injection at all Q values to investigate the evolution of injection pressure (P_{in}) before and after the breakthrough. The pressure was measured near the inlet using a pressure sensor (Keyence, AP-12S). Fig. 11 indicates the evolution of P_{in} with the injection PV at different Q values. The P_{in} was evaluated as an average pressure over time for each injection PV. The P_{in} increased in two- and single-phase flow experiments with an increase in Q or LogCa. The increase in the pressure gradient of the injected fluid or fluid–fluid interface influences the remobilization or migration of particles. For strong drainage (Fig. 11(A)) and strong imbibition (Fig. 11(B)), the injection pressure drastically increased with the injected volume and sharply decreased after the breakthrough. However, the P_{in} remained stable after the breakthrough in single-phase flow experiments (Fig. 11(C)). This indicates the impact of interface movement on injection pressure during fluid-particle interactions for two-phase flow compared with single-phase flow. The rapid increase in injection pressure and fluctuation with the injected volume at $Q = 0.1$ mL/h (Fig. 11(A)) might be caused by particle accumulation or clogging in random pore networks owing to interface expansion (Figs. 5(A) and (B)).

It is important to estimate the heterogeneity of the medium (i.e., permeability reduction) caused by the clogging or bridging of fine particles in the pore channels for CO_2 injectivity assessment in heterogeneous formation. In the present two-phase flow experiments, evaluating the absolute or relative permeability change during transport was complicated because the system had not attained a steady state. As is the case of strong drainage at $Q = 0.1$ mL/h (Fig. 11(A)), the accumulation of fine particles in random pore networks due to the interface expansion between fluid phases induced fluctuations in injection pressure even after the breakthrough, indicating that fine particles were continually clogged or displaced to any regions during continuous injection.

4. Summary and conclusions

The particle migration and 3D fluid–fluid displacement of the immiscible two-phase flow systems in 3D heterogeneous porous media were visualized using a microfocus X-ray CT scanner. The experimental conditions were $-7.476 \leq \text{Log}Ca \leq -4.777$ and $\text{Log}M = -0.8687$. The characteristics of fluid–fluid displacement at different injection flow rates and wettability conditions were investigated, and the combined effects of interfacial tension and viscous force on particle migration are explained. Single-phase flow experiments were conducted to elucidate the effect of interfacial tension compared with two-phase flow experiments. The findings of this study are as follows.

For strong drainage, at a low Q or LogCa, particles migrate with interface expansion in the entire medium and accumulate in random pore networks, potentially inducing heterogeneity and fluid flow characteristics. As Q or LogCa increases, the combined effects of interfacial tension and viscous force promote particle movement. The 3D structure of the invading fluid shifts from a compact structure to a streak-like structure as LogCa increases, decreasing the average saturation in the system. The accumulation of particles by the interface expansion in random pore networks increases the injection pressure.

In strong imbibition, particle migration proceeds with the film formations of the invading fluid surrounding the particle surfaces. The combined effects of interfacial tension and viscous force are less

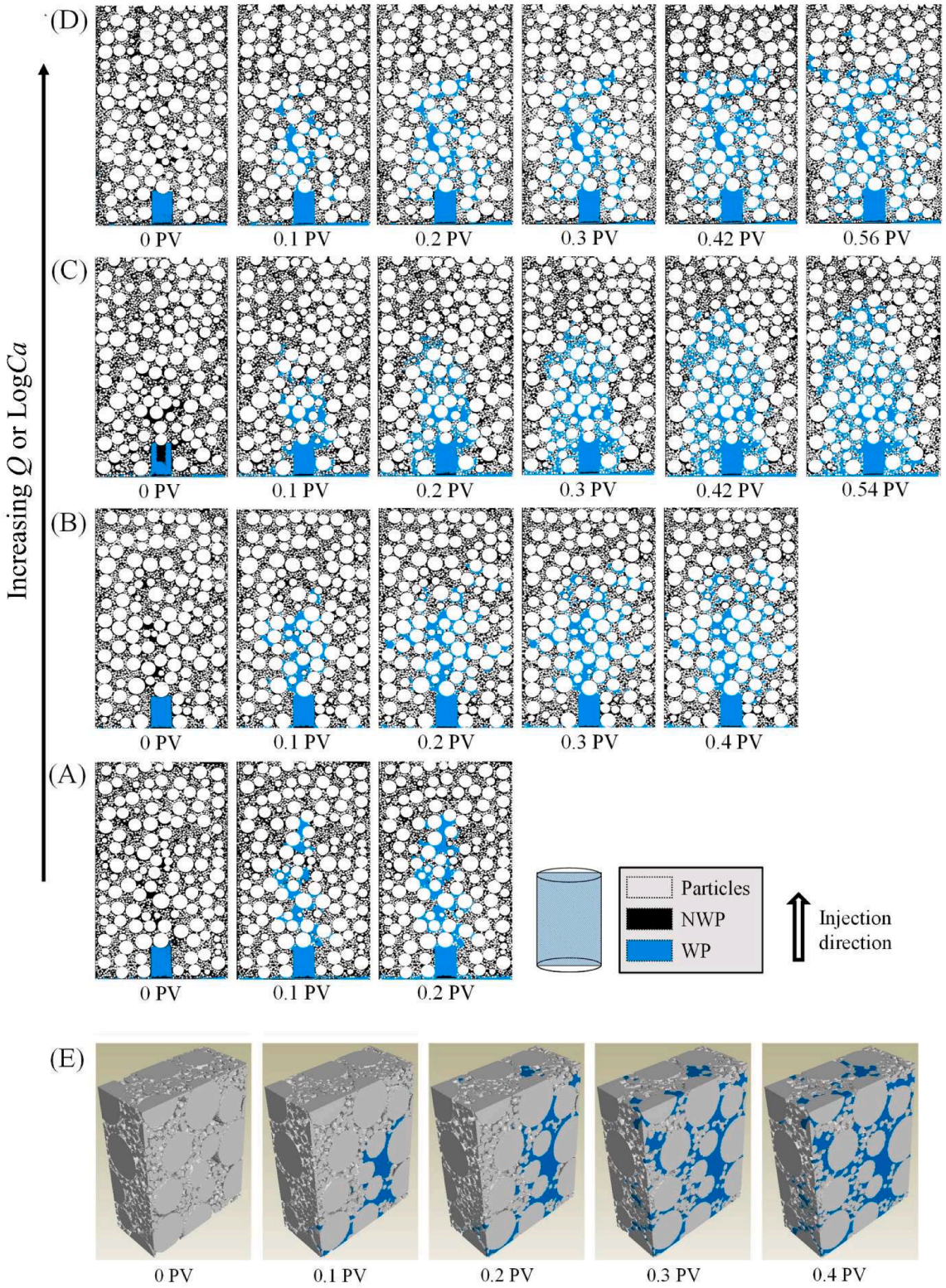

Fig. 8. Vertical cross-sectional images of invading WP after each injection into the packed bed at (A) 0.1, (B) 1, (C) 10, and (D) 50 mL/h (top panels). The white, blue, and black colors denote the particle, WP, and NWP, respectively. The horizontal cross-sectional images of fluid–fluid displacement for imbibition experiments at all Q values are shown in Figs. 15S–18S. The bottom panels show the 3D cross-sectional views of the invasion front behavior of the invading phase at (E) $Q = 1$ mL/h randomly taken near the front with a region of interest of $1.28 \times 3.92 \times 4.24$ mm^3. The gray and blue colors denote the particle and WP phases; the empty pore represents the NWP.

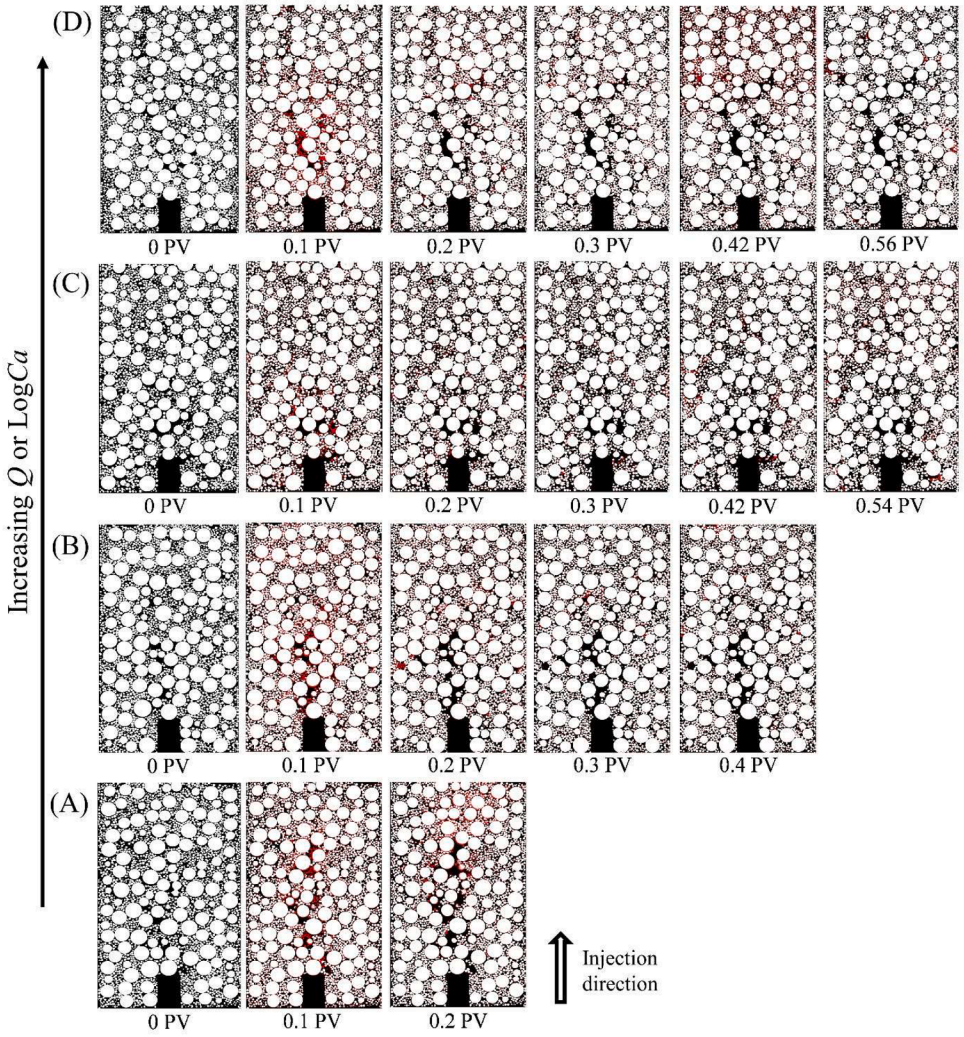

Fig. 9. Vertical cross-sectional images of particle migration with injection pore volume for imbibition displacement at various Q values (A) 0.1, (B) 1, (C) 10, and (D) 50 mL/h. The red color denotes the particle movement compared with its initial position after each injection. The horizontal cross-sectional images of particle migration for imbibition experiments at all Q values are shown in Figs. 19S –22S.

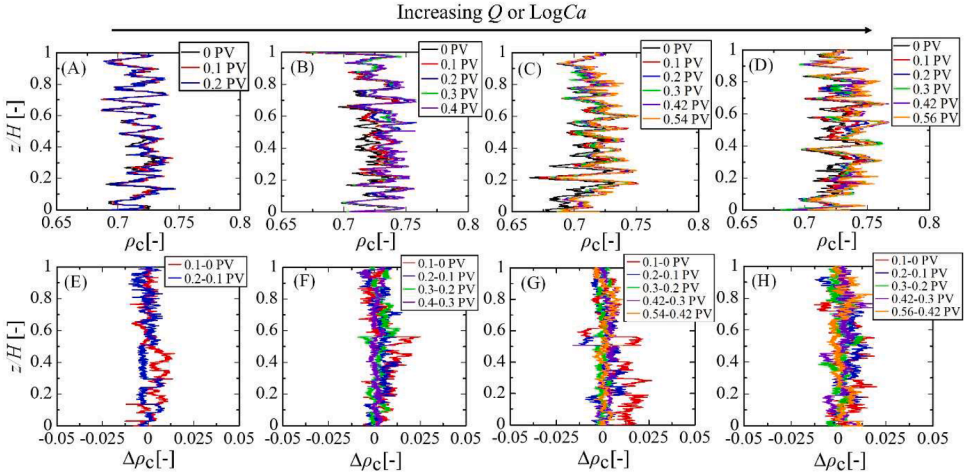

Fig. 10. Vertical profiles of ρ_c and $\Delta\rho_c$ along the packed bed. The top panels show the distribution of the ρ_c of particles along the packed bed at various Q values (A) 0.1, (B) 1, (C) 10, and (D) 50 mL/h. The bottom panels show the $\Delta\rho_c$ for each injection volume of the IP at (E) 0.1, (F) 1, (G) 10, and (H) 50 mL/h. Q (flow rate) or LogCa increased from left to right (black arrow).

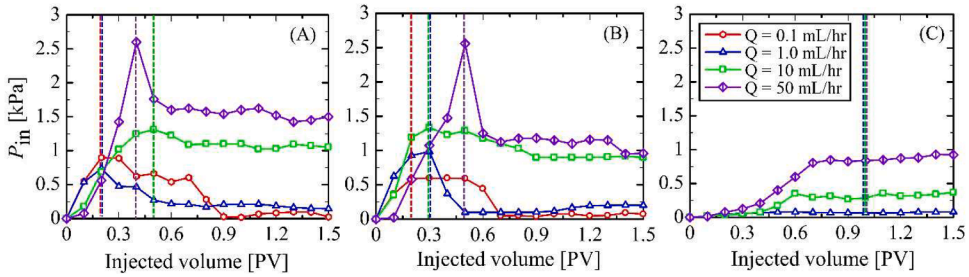

Fig. 11. Evolution of injection pressure at different flow rates for (A) strong drainage, (B) strong imbibition, and (C) single-phase flow experiments. The colored dash lines indicate the breakthrough at its injection volume.

significant than in strong drainage because of the presence of film flows that reduce the strength of the interfacial tension effect at the interface. The 3D structure of the invading fluid transforms from a streak-like structure to a more compact structure with an increase in Log*Ca*, increasing the average saturation of the system.

Our findings provide a better understanding of how particle migration proceeds with the invasion of the injected fluid and the transition of the 3D structure of the injected fluid at different injection velocities when medium wettability is altered, which are beneficial for the better system design of CCS, enhanced oil recovery, etc. However, the reported results in this work may not be sufficient to fully account for the effects of single- and two-phase flow-induced all mechanisms of particle migration and heterogeneity. Further studies and detailed quantitative analysis are necessary to elucidate the effects of viscosity ratio and particle mixture ratio on particle migration in single- and two-phase flow and the effects of heterogeneity. Furthermore, it is also necessary to verify the observation of film or corner flows with theoretical frameworks.

CRediT authorship contribution statement

Sotheavuth Sin: Writing – review & editing, Writing – original draft, Visualization, Methodology, Investigation, Formal analysis, Data curation. **Muhammad Nasir:** Visualization, Formal analysis. **Kailin Wang:** Validation, Formal analysis. **Aninditya Patmonoaji:** Validation, Software. **Wilson Susanto:** Validation, Formal analysis. **Bowen Wang:** Validation, Formal analysis. **Shintaro Matsushita:** Resources, Project administration. **Tetsuya Suekane:** Writing – review & editing, Supervision, Funding acquisition, Conceptualization.

Declaration of competing interest

The authors declare that they have no known competing financial interests or personal relationships that could have appeared to influence the work reported in this paper.

Acknowledgements

We thank the anonymous reviewers for their constructive comments and corrections, which have greatly improved this manuscript. The authors acknowledge the support from JSPS KAKENHI (Grant number. 22H03770). S. Sin also acknowledges the scholarship support from the Japan International Cooperation Agency for the study at the Institute of Science Tokyo.

Supplementary materials

Supplementary material associated with this article can be found, in the online version, at doi:10.1016/j.advwatres.2025.104998.

Data availability

Data will be made available on request.

References

Andrew, M., Bijeljic, B., Blunt, M., 2015. Reservoir condition pore-scale imaging of multiple fluid phases using X-ray microtomography. J. Vis. Exp. 1–10. https://doi.org/10.3791/52440.

Alhammadi, A.M., Gao, Y., Akai, T., Blunt, M.J., Bijeljic, B., 2020. Pore-scale X-ray imaging with measurement of relative permeability, capillary pressure and oil recovery in a mixed-wet micro-porous carbonate reservoir rock. Fuel 268, 117018. https://doi.org/10.1016/j.fuel.2020.117018.

Almutairi, A., Saira, S., Wang, Y., Le-Hussain, F., 2023. Effect of fines migration on oil recovery from carbonate rocks. Adv. Geo-Energy Res. 8, 61–70. https://doi.org/10.46690/AGER.2023.04.06.

Berg, S., Ott, H., Klapp, S.A., Schwing, A., Neiteler, R., Brussee, N., Makurat, A., Leu, L., Enzmann, F., Schwarz, J.O., Kersten, M., Irvine, S., Stampanoni, M., 2013. Real-time 3D imaging of Haines jumps in porous media flow. Proc. Natl. Acad. Sci. U.S.A. 110, 3755–3759. https://doi.org/10.1073/pnas.1221373110.

Boronin, S.A., Osiptsov, A.A., 2014. Effects of particle migration on suspension flow. Fluid Dyn. 49, 208–221. https://doi.org/10.1134/S0015462814020094.

Carbillet, L., Heap, M.J., Baud, P., Wadsworth, F.B., Reuschlé, T., 2022. The Influence of grain zize distribution on mechanical compaction and compaction localization in porous rocks. J. Geophys. Res. Solid Earth 127, 1–22. https://doi.org/10.1029/2022JB025216.

Chen, Y., Saeedi, A., Xie, Q., 2023. Interfacial interactions of CO2-brine-rock system in saline aquifers for CO2 geological storage: a critical review. Int. J. Coal Geol. 274, 104272. https://doi.org/10.1016/j.coal.2023.104272.

Chen, Y.F., Fang, S., Wu, D.S., Hu, R., 2017. Visualizing and quantifying the crossover from capillary fingering to viscous fingering in a rough fracture. Water Resour. Res. 53, 7756–7772. https://doi.org/10.1002/2017WR021051.

Chevalier, C., Lindner, A., Leroux, M., Clément, E., 2009. Morphodynamics during air injection into a confined granular suspension. J. Nonnewton. Fluid Mech. 158, 63–72. https://doi.org/10.1016/j.jnnfm.2008.07.007.

Civan, F., 2010. Non-isothermal permeability impairment by fines migration and deposition in porous media including dispersive transport. Transp. Porous Media 85, 233–258. https://doi.org/10.1007/s11242-010-9557-0.

Cooper, L.J., Daly, K.R., Hallett, P.D., Naveed, M., Koebernick, N., Bengough, A.G., George, T.S., Roose, T., 2017. Fluid flow in porous media using image-based modelling to parametrize Richards' equation. Proc. R. Soc. A Math. Phys. Eng. Sci. 473, 20170178. https://doi.org/10.1098/rspa.2017.0178.

Constantinides, G.N., Payatakes, A.C., 2000. Effects of precursor wetting films in immiscible displacement through porous media. Transp. Porous Media 38, 291–317. https://doi.org/10.1023/A:1006557114996.

Derbyshev, D.Y., Boronin, S.A., Ovchinnikov, G.V., Osiptsov, A.A., 2024. On the efficient non-linear solver for hydraulic fracturing and well cementing simulations based on Anderson acceleration. Pet. Sci. 21, 3237–3257. https://doi.org/10.1016/j.petsci.2024.06.013.

Eriksen, F.K., Toussaint, R., Måløy, K.J., Flekkøy, E.G., 2015a. Invasion patterns during two-phase flow in deformable porous media. Front. Phys. 3, 1–15. https://doi.org/10.3389/fphy.2015.00081.

Eriksen, J.A., Marks, B., Sandnes, B., Toussaint, R., 2015b. Bubbles breaking the wall: two-dimensional stress and stability analysis. Phys. Rev. E - Stat. Nonlinear, Soft Matter Phys. 91, 1–10. https://doi.org/10.1103/PhysRevE.91.052204.

Ge, J., Zhang, X., Le-Hussain, F., 2022. Fines migration and mineral reactions as a mechanism for CO_2 residual trapping during CO_2 sequestration. Energy 239, 122233. https://doi.org/10.1016/j.energy.2021.122233.

Glass, R.J., Rajaram, H., Detwiler, R.L., 2003. Immiscible displacements in rough-walled fractures: competition between roughening by random aperture variations and smoothing by in-plane curvature. Phys. Rev. E - Stat. Physics, Plasmas, Fluids, Relat. Interdiscip. Top. 68, 1–6. https://doi.org/10.1103/PhysRevE.68.061110.

Han, G., Kwon, T.H., Lee, J.Y., Jung, J., 2020. Fines migration and pore clogging induced by single- and two-phase fluid flows in porous media: from the perspectives of particle detachment and particle-level forces. Geomech. Energy Environ. 23, 100131. https://doi.org/10.1016/j.gete.2019.100131.

Han, G., Kwon, T.H., Lee, J.Y., Kneafsey, T.J., 2018. Depressurization-induced fines migration in sediments containing methane hydrate: x-Ray computed tomography imaging experiments. J. Geophys. Res. Solid Earth 123, 2539–2558. https://doi.org/10.1002/2017JB014988.

Herring, A.L., Middleton, J., Walsh, R., Kingston, A., Sheppard, A., 2017. Flow rate impacts on capillary pressure and interface curvature of connected and disconnected fluid phases during multiphase flow in sandstone. Adv. Water Resour. 107, 460–469. https://doi.org/10.1016/j.advwatres.2017.05.011.

Holtzman, R., Szulczewski, M.L., Juanes, R., 2012. Capillary fracturing in granular media. Phys. Rev. Lett. 108. https://doi.org/10.1103/PhysRevLett.108.264504.

House, K.Z., Schrag, D.P., Harvey, C.F., Lackner, K.S., 2006. Permanent carbon dioxide storage in deep-sea sediments. Proc. Natl. Acad. Sci. U.S.A. 103, 12291–12295. https://doi.org/10.1073/pnas.0605318103.

Hu, R., Wan, J., Kim, Y., Tokunaga, T.K., 2017. Wettability effects on supercritical CO_2–brine immiscible displacement during drainage: pore-scale observation and 3D simulation. Int. J. Greenh. Gas Control 60, 129–139. https://doi.org/10.1016/j.ijggc.2017.03.011.

Hu, Y., Patmonoaji, A., Zhang, C., Suekane, T., 2020. Experimental study on the displacement patterns and the phase diagram of immiscible fluid displacement in three-dimensional porous media. Adv. Water Resour. 140, 103584. https://doi.org/10.1016/j.advwatres.2020.103584.

Huang, F., Kang, Y., You, L., Li, X., You, Z., 2018. Massive fines detachment induced by moving gas-water interfaces during early stage two-phase flow in coalbed methane reservoirs. Fuel 222, 193–206. https://doi.org/10.1016/j.fuel.2018.02.142.

Idowu, N.A., Blunt, M.J., 2010. Pore-scale modelling of rate effects in waterflooding. Transp. Porous Media 83, 151–169. https://doi.org/10.1007/s11242-009-9468-0.

Iraji, S., De Almeida, T.R., Munoz, E.R., Basso, M., Vidal, A.C., 2024. The impact of heterogeneity and pore network characteristics on single and multi-phase fluid propagation in complex porous media: an X-ray computed tomography study. Pet. Sci. 21, 1719–1738. https://doi.org/10.1016/j.petsci.2024.01.015.

Islam, A., Chevalier, S., Salem, I.B., Bernabe, Y., Juanes, R., Sassi, M., 2014. Characterization of the crossover from capillary invasion to viscous fingering to fracturing during drainage in a vertical 2D porous medium. Int. J. Multiph. Flow 58, 279–291. https://doi.org/10.1016/j.ijmultiphaseflow.2013.10.002.

Jung, J., Cao, S.C., Shin, Y.H., Al-Raoush, R.I., Alshibli, K., Choi, J.W., 2018. A microfluidic pore model to study the migration of fine particles in single-phase and multi-phase flows in porous media. Microsyst. Technol. 24, 1071–1080. https://doi.org/10.1007/s00542-017-3462-1.

Ke, L., Takahashi, A., 2014. Experimental investigations on suffusion characteristics and its mechanical consequences on saturated cohesionless soil. Soils Found 54, 713–730. https://doi.org/10.1016/j.sandf.2014.06.024.

Kézdi, A., 1979. Soil Physics: Selected Topics. Elsevier Scientific Publishing Co., Amsterdam.

Krummel, A.T., Datta, S.S., Munster, S., Weitz, D.A., 2012. Visualizing mulitphase flow and trapped fluid configurations in a model three-dimensional porous medium. AIChE J 59, 215–228. https://doi.org/10.1002/aic.

Ladd, R.S., 1978. Preparing test specimens using under compaction. Geotech. Test. J. 1 (1), 16. https://doi.org/10.1520/GTJ10364J.

Lenormand, R., Touboul, E., Zarcone, C., 1988. Numerical models and experiments on immiscible displacements in porous media. J. Fluid Mech. 189, 165–187. https://doi.org/10.1017/S0022112088000953.

Levaché, B., Bartolo, D., 2014. Revisiting the Saffman-Taylor experiment: imbibition patterns and liquid-entrainment transitions. Phys. Rev. Lett. 113, 1–5. https://doi.org/10.1103/PhysRevLett.113.044501.

Liu, H., Zhang, Y., Valocchi, A.J., 2015. Lattice boltzmann simulation of immiscible fluid displacement in porous media: homogeneous versus heterogeneous pore network. Phys. Fluids 27. https://doi.org/10.1063/1.4921611.

Meng, Y., Li, W., Juanes, R., 2023. Crossover from viscous fingering to fracturing in cohesive wet granular media: a photoporomechanics study. Soft Matter 19, 7136–7148. https://doi.org/10.1039/d3sm00897e.

Moebius, F., Or, D., 2012. Interfacial jumps and pressure bursts during fluid displacement in interacting irregular capillaries. J. Colloid Interface Sci. 377, 406–415. https://doi.org/10.1016/j.jcis.2012.03.070.

Muharrik, M., Suekane, T., Patmonoaji, A., 2018. Effect of buoyancy on fingering growth activity in immiscible two-phase flow displacements. J. Fluid Sci. Technol. 13, 1–12. https://doi.org/10.1299/jfst.2018jfst0006.

Nelson, P.H., 2004. Permeability–porosity data sets for sandstones. Lead. Edge, 23, 1143–1144. https://doi.org/10.1190/1.1813360.

Nguyen, C.D., Benahmed, N., Andò, E., Sibille, L., Philippe, P., 2019. Experimental investigation of microstructural changes in soils eroded by suffusion using X-ray tomography. Acta Geotech 14, 749–765. https://doi.org/10.1007/s11440-019-00787-w.

Patmonoaji, A., Muharrik, M., Hu, Y., Zhang, C., Suekane, T., 2020a. Three-dimensional fingering structures in immiscible flow at the crossover from viscous to capillary fingering. Int. J. Multiph. Flow 122. https://doi.org/10.1016/j.ijmultiphaseflow.2019.103147.

Patmonoaji, A., Tsuji, K., Suekane, T., 2020b. Pore-throat characterization of unconsolidated porous media using watershed-segmentation algorithm. Powder Technol. 362, 635–644. https://doi.org/10.1016/j.powtec.2019.12.026.

Patzek, T.W., 2001. Verification of a complete pore network simulator of drainage and imbibition. SPE-59312-MS. https://doi.org/10.2118/59312-MS.

Payton, R.L., Fellgett, M., Clark, B.L., Chiarella, D., Kingdon, A., Hier-Majumder, S., 2020. Pore-scale assessment of subsurface carbon storage potential: implications for the UK geoenergy observatories project. Pet. Geosci. 27. https://doi.org/10.1144/petgeo2020-092.

Peng, S., Hu, Q., Dultz, S., Zhang, M., 2012. Using X-ray computed tomography in pore structure characterization for a Berea sandstone: resolution effect. J. Hydrol. 472–473, 254–261. https://doi.org/10.1016/j.jhydrol.2012.09.034.

Prasomsri, J., Takahashi, A., 2021. Experimental study on suffusion under multiple seepages and its impact on undrained mechanical responses of gap-graded soil. Soils Found 61, 1660–1680. https://doi.org/10.1016/j.sandf.2021.10.003.

Qanbari, F., Pooladi-Darvish, M., Tabatabaie, S.H., Gerami, S., 2011. Storage of CO2 as hydrate beneath the ocean floor. Energy Procedia 4, 3997–4004. https://doi.org/10.1016/j.egypro.2011.02.340.

Rabbani, A., Ayatollahi, S., Kharrat, R., Dashti, N., 2016. Estimation of 3-D pore network coordination number of rocks from watershed segmentation of a single 2-D image. Adv. Water Resour. 94, 264–277. https://doi.org/10.1016/j.advwatres.2016.05.020.

Russell, T., Wong, K., Zeinijahromi, A., Bedrikovetsky, P., 2018. Effects of delayed particle detachment on injectivity decline due to fines migration. J. Hydrol. 564, 1099–1109. https://doi.org/10.1016/j.jhydrol.2018.07.067.

Schrag, D.P., 2007. Preparing to capture carbon. Science 315, 812–813. https://doi.org/10.1126/science.1137632.

Shang, J., Flury, M., Deng, Y., 2009. Force measurements between particles and the air-water interface: implications for particle mobilization in unsaturated porous media. Water Resour. Res. 45, 1–14. https://doi.org/10.1029/2008WR007384.

Sharma, M.M., Chamoun, H., Sarma, D.S.H.S.R., Schechter, R.S., 1992. Factors controlling the hydrodynamic detachment of particles from surfaces. J. Colloid Interface Sci. 149, 121–134. https://doi.org/10.1016/0021-9797(92)90398-6.

She, Y., Wang, W., Hu, Y., Mahardika, M.A., Nasir, M., Zhang, C., Patmonoaji, A., Matsushita, S., Suekane, T., 2022. Pore-scale investigation on microemulsion-based quasi-miscible flooding for EOR in water-wet/oil-wet reservoirs: a 3D study by X-ray microtomography. J. Pet. Sci. Eng. 216, 110788. https://doi.org/10.1016/j.petrol.2022.110788.

Shiga, M., Morishita, T., Sorai, M., 2023. Interfacial tension of carbon dioxide - water under conditions of CO2 geological storage and enhanced geothermal systems: a molecular dynamics study on the effect of temperature. Fuel 337, 127219. https://doi.org/10.1016/j.fuel.2022.127219.

Tang, G.Q., Morrow, N.R., 1999. Influence of brine composition and fines migration on crude oil/brine/rock interactions and oil recovery. J. Pet. Sci. Eng. 24, 99–111. https://doi.org/10.1016/S0920-4105(99)00034-0.

Tekseth, R.K., Mirzaei, F., Lukic, B., Chattopadhyay, B., Breiby, W.D., 2023. Mutiscale drainage dynamics with Haines jumps monitored by stroboscopic 4D X-ray microscopy. Proc. Natl. Acad. Sci. U.S.A. 121, 1–8. https://doi.org/10.1073/pnas.

Teng, Y., Zhang, D., 2018. Long-term viability of carbon sequestration in deep-sea sediments. Sci. Adv. 4, 1–8. https://doi.org/10.1126/sciadv.aao6588.

Wang, K., Matsushita, S., Yamashita, S., Nasir, M., Suekane, T., 2024. Energy transfer process during Haines jumps and meniscus reconfiguration with a high-density and viscosity ratio. Int. J. Heat Mass Transf. 230, 125749. https://doi.org/10.1016/j.ijheatmasstransfer.2024.125749.

Wang, Y., Almutairi, A.L.Z., Bedrikovetsky, P., Timms, W.A., Privat, K.L., Bhattacharyya, S.K., Le-Hussain, F., 2022a. In-situ fines migration and grains redistribution induced by mineral reactions – implications for clogging during water injection in carbonate aquifers. J. Hydrol. 614, 128533. https://doi.org/10.1016/j.jhydrol.2022.128533.

Wang, Y., Bedrikovetsky, P., Yin, H., Othman, F., Zeinijahromi, A., Le-Hussain, F., 2022b. Analytical model for fines migration due to mineral dissolution during CO2 injection. J. Nat. Gas Sci. Eng. 100, 104472. https://doi.org/10.1016/j.jngse.2022.104472.

Xie, Q., Saeedi, A., Delle Piane, C., Esteban, L., Brady, P.V., 2017. Fines migration during CO2 injection: experimental results interpreted using surface forces. Int. J. Greenh. Gas Control 65, 32–39. https://doi.org/10.1016/j.ijggc.2017.08.011.

Xie, Z., Wang, S., Shen, Y., 2023. Roles of clusters in the migration of fines through porous media. Chem. Eng. Sci. 265, 118217. https://doi.org/10.1016/j.ces.2022.118217.

Xu, Y., Ye, X., Du, X., 2024. Microscopic mechanism of particle clogging in porous media during managed aquifer recharge: from X-ray computed tomography (CT) imaging to numerical modelling. Hydrol Process 38. https://doi.org/10.1002/hyp.70002.

Yang, Z., Méheust, Y., Neuweiler, I., Hu, R., Niemi, A., Chen, Y.F., 2019. Modeling immiscible two-phase flow in rough fractures from capillary to viscous fingering. Water Resour. Res. 55, 2033–2056. https://doi.org/10.1029/2018WR024045.

Yang, Z., Neuweiler, I., Méheust, Y., Fagerlund, F., Niemi, A., 2016. Fluid trapping during capillary displacement in fractures. Adv. Water Resour. 95, 264–275. https://doi.org/10.1016/j.advwatres.2015.07.015.

Zeinijahromi, A., Farajzadeh, R., Bruining, J., Bedrikovetsky, P., 2016. Effect of fines migration on oil-water relative permeability during two-phase flow in porous media. Fuel 176, 222–236. https://doi.org/10.1016/j.fuel.2016.02.066.

Zhang, C., Oostrom, M., Wietsma, T.W., Grate, J.W., Warner, M.G., 2011. Influence of viscous and capillary forces on immiscible fluid displacement: pore-scale experimental study in a water-wet micromodel demonstrating viscous and capillary fingering. Energy Fuels 25, 3493–3505. https://doi.org/10.1021/ef101732k.

Zhao, B., MacMinn, C.W., Juanes, R., 2016. Wettability control on multiphase flow in patterned microfluidics. Proc. Natl. Acad. Sci. U.S.A. 113, 10251–10256. https://doi.org/10.1073/pnas.1603387113.

Zhu, S.Y., Peng, X.L., Du, Z.M., Wang, C.W., Deng, P., Mo, F., Lei, Y., Wang, M., 2017. Modeling of coal fine migration during CBM production in high-rank coal. Transp. Porous Media 118, 65–83. https://doi.org/10.1007/s11242-017-0847-7.

Zoback, M.D., Gorelick, S.M., 2012. Earthquake triggering and large-scale geologic storage of carbon dioxide. Proc. Natl. Acad. Sci. U.S.A. 109, 10164–10168. https://doi.org/10.1073/pnas.1202473109.